31st Congress of the International Council of the Aeronautical Sciences

Belo Horizonte, Brazil; September 09-14, 2018

NUMERICAL SIMULATION OF ICE ACCRETION INFLUENCED BY AN ANTI-ICING HEATING SYSTEM

Krzysztof Szilder*, Edward Lozowski**
***Aerospace, National Research Council, Ottawa, Ontario, Canada**
****University of Alberta, Edmonton, Alberta, Canada**

Keywords: *icing, de-icing, anti-icing, supercooled drops, simulation*

Abstract

Over the last two decades, we have developed an original icing modelling capability called the "morphogenetic" approach, based on a discrete formulation and simulation of ice formation physics. Recently, we have extended the predictive capabilities of the model to include an analysis of the consequences of a thermal anti-icing system on the ice accretion process and the resulting runback ice formation. When the anti-icing system does not evaporate all of the impinging drops, the ice forming downstream from the heated region may have a complex shape. Although aerodynamic penalties due to this ice have not yet been computed, the resulting ice shapes suggest that the aerodynamic penalties may be unacceptable when anti-icing heating is insufficient. This situation could potentially be hazardous if fixed heating is applied while the environmental conditions are rapidly changing.

1 Introduction

Atmospheric icing occurs when airborne supercooled water drops freeze on objects they encounter. This process is especially hazardous to aircraft when the ice build-up changes the stability and control characteristics of the aerodynamic surfaces. In order to avoid aerodynamic performance degradation, anti-icing and de-icing systems may be implemented. The anti-icing strategy focuses on preventing ice formation on "protected" surfaces, while the de-icing approach involves periodic removal of already formed ice. Thermal anti-icing systems have two regimes: 1. Evaporative, when there is enough heat delivered to evaporate all impinging water; and 2. Wet, when some water evaporates and some runs back to freeze downstream on unprotected surfaces. An ability to numerically model the buildup of runback ice is essential to the prediction and mitigation of its associated aerodynamic penalties. Numerical simulations can also assist in the optimization of icing wind tunnels tests and a reduction in the need for expensive, time consuming and dangerous in-flight tests.

There have been numerous publications describing problems related to thermal anti-icing systems. Some of the published work has focused on laboratory experiments of runback ice formation, e.g., [1-4]; some on the aerodynamic penalties of runback ice accretion, e.g., [5]; and some on optimization of anti-icing systems [6]. However, the issue of predicting the detailed shapes of the resulting runback ice accretions has not been treated adequately. The objective of this work is to fill this gap. This is critical since the particulars of the residual ice accretion shape are crucial in determining the aerodynamic penalties that result from insufficient performance of a thermal anti-icing system. Examination of the actual aerodynamic penalties will be addressed in our future work.

At the National Research Council (NRC), we have developed a unique icing modelling capability called the "morphogenetic" approach, which is based on a discrete formulation and simulation of ice formation physics. The development of this approach for the prediction of 2D ice accretion shapes in the aerospace industry is explained in [7]. Recent 3D modelling advances are described in [8]. In this

work, we extend the applicability of the model to include prediction of the consequences of anti-icing heating on the resulting ice accretion shape.

The objective of this contribution is to demonstrate that the morphogenetic modelling approach can be used to predict geometrically realistic ice shapes occurring on or behind anti-icing heating devices. In future work, we will compare these model predictions with wind tunnel experiments.

2 Model Description

Three principal physical processes influence ice formation, each with a corresponding numerical module: airflow is determined using computational fluid dynamics (CFD) tools, drop trajectories using a drop trajectory solver, and drop motion and freezing on the surface using NRC's morphogenetic approach. In the present work, the flow solution is two-dimensional (but not the icing), and it does not vary along the span [9]. The air velocity field was used as input to a Lagrangian drop trajectory solver, developed in-house at NRC [10]. Computation of the drop trajectories (also two-dimensional) and drop impact locations leads to a determination of the local collision efficiency distribution for the clean airfoil; this is passed to the morphogenetic model. It should be emphasized that, in this study, the computation of the airflow and drop trajectories was performed only once for the clean wing. Consequently, the results do not account for the feedback of the growing ice accretion on the airflow, drop trajectories and heat transfer.

In the morphogenetic ice accretion model, the mass flux of impinging droplets is divided into fluid elements that are typically larger than individual cloud drops. Consequently, we think of individual fluid elements as consisting of ensembles of cloud drops, all of which have identical histories. A three-dimensional, cubic lattice defines the accretion domain. By building the accretion one element at a time on this lattice, the morphogenetic model emulates the time evolution of the accretion shape in a way that mimics the real world and takes into account real-world physics. In our model, the fluid elements are allowed to impact randomly on the wing surface or on the existing ice structure in such a way that their mass distribution is consistent with the collision efficiency distribution, computed for a single drop size on a clean wing.

The methodology used to compute the downstream motion and freezing of fluid elements on the surface is the same as the procedure already described for two-dimensional [7] and three-dimensional [8,10] configurations. In the present work, an anti-icing heating module has been implemented by adding this additional heat flux to the energy equation. This equation is then solved to determine the rate of ice formation on a wing surface. The results presented and discussed in this paper were obtained assuming uniform heating in our assumed anti-icing domain.

At each step of a fluid element's motion on the surface, a normalized random number is generated and compared with the local probability of freezing, which is, in turn, determined from the surface energy and mass conservation equations. Depending on the outcome of this comparison, a fluid element either continues its motion or it freezes. The model is sequential, so that as soon as a particular fluid element freezes, the behavior of the next fluid element is considered.

The results presented in this paper were obtained for a grid cell size of 400×400×400 μm (this is also the size of individual fluid elements) and a morphogenetic model domain of 600×300×600 elements, which is equivalent to 24×12×24 cm in the chordwise, spanwise and vertical directions, respectively. The grid size/fluid element size was chosen as a compromise between model precision and computational effort. The total number of impinging fluid elements is determined by the freestream velocity, liquid water content, fluid element size, duration of the icing event, and spatial distribution of the collision efficiency.

3 Partial Model Validation

The morphogenetic model underwent an extensive validation process using a variety of experimental data with a focus on ice thickness distribution. In this paper, we will show only two validation results demonstrating the influence of an anti-icing system on ice accretion shape. The following parameter values, typical for aircraft descent, were assumed [2, 11]: airfoil NACA0018, chord length 0.4572 m, altitude 3050 m, speed 92.8 m/s, angle of attack 0°, static air temperature - 14°C, liquid water content 0.35 g/m^3, and median volume droplet diameter 20 µm. The simulated three-dimensional ice shape and three cross-sections (depicted by different shades of blue) are compared with experimental results (depicted in red) in Figures 1a and 1b.

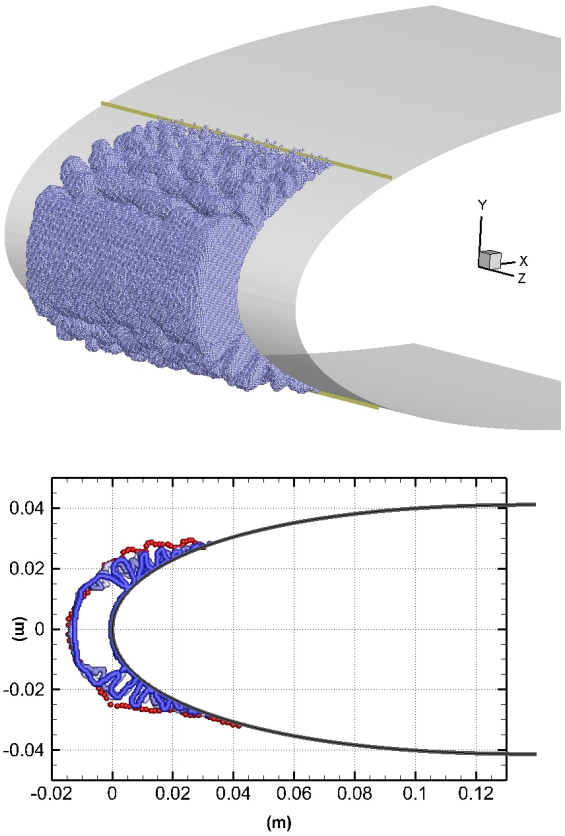

Figure 1a. Comparison between the model simulation and experimental cross-sections, without anti-icing heating.

When there is no anti-icing heating, agreement between the predicted ice shape and experimental result is satisfactory, Figure 1a. An area of comparatively uniform ice layer at the leading edge vicinity is followed downstream by irregular, rough rime ice of diminishing thickness. The drop impingement limit is depicted by dark yellow lines, and ice does not form downstream.

When anti-icing heating of 5.6 kW/m^2 is applied over the area depicted in red in Figure 1b, some impinging drops flow downstream without freezing and some evaporate. An ice accretion forms only downstream from the heated region. In this case, the agreement between predicted ice shape cross-sections and their experimental counterparts is also satisfactory.

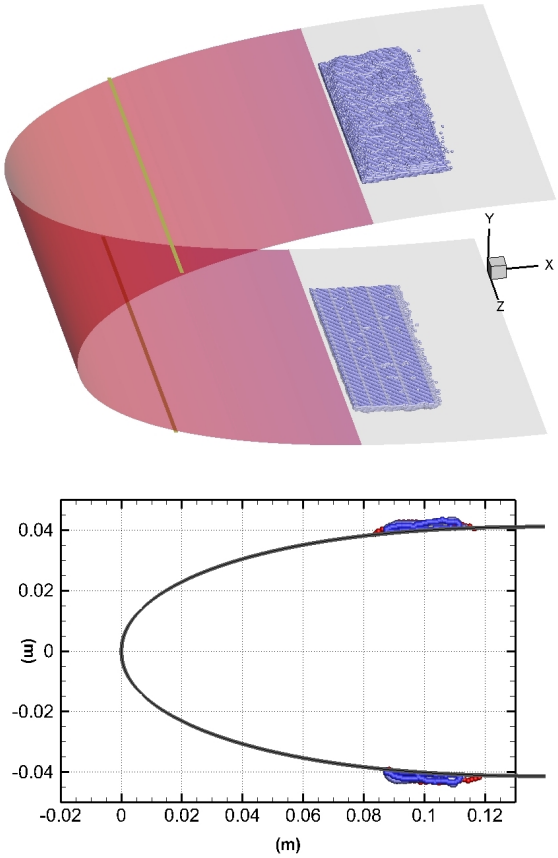

Figure 1b. Comparison between the model simulations and experimental cross-sections with anti-icing heating of 5.6 kW/m^2.

4 Results and Discussion

Three sets of icing conditions that represent different aircraft icing scenarios were selected: Warm Hold, an aircraft hold at a relatively warm air temperature; Descent, an aircraft

	altitude (m)	speed (m/s)	AOA (^{o})	T_{AS} (^{o}C)	LWC (g/m^3)	MVD (μm)
Warm Hold	4570	92.8	0	-9	0.50	20
Descent	3050	92.8	0	-14	0.35	20
Cold Hold	4570	92.8	0	-30	0.24	20

Table 1. Examined icing scenarios.

descent at an intermediate air temperature; and Cold Hold, a hold at a relatively low air temperature. The icing conditions associated with these scenarios are listed in Table 1. The values were taken from [2]. AOA is angle of attack, T_{AS} is static air temperature, LWC is liquid water content, and MVD is median volume droplet diameter. An NRC-designed airfoil of 1 m chord was considered and the duration of the icing event was assumed to be 10 min.

4.1 Airflow and Drop Trajectories Prediction

Computations of the airflow and drop trajectories were performed prior to considering ice formation. Figure 2 depicts a sample of results assuming Descent conditions. Contours of horizontal velocity magnitude and velocity vectors are shown in Figure 2a. A sample of drop trajectories (dark red lines) and their impingement locations (blue dots) is shown in the vicinity of the leading edge on Figure 2b. The computed airflow near the surface and the intensity and location of drop impingement were used as an input parameters to the morphogenetic ice prediction module.

4.2 Ice Accretion Prediction

Ice accretions were computed for three values of anti-icing heating: 0, 4 and 20 kW/m^2. The heat was applied uniformly on the anti-iced section of the wing surface. The blue lines shown in Figure 3 on the wing indicate the drop impingement limits, while the reddish surface indicates the anti-icing heated region. The total length of this heated region is 16 cm and the displayed section of the ice accretion is 6 cm wide. Figure 3 shows the ice accretion shapes for the three sets of conditions.

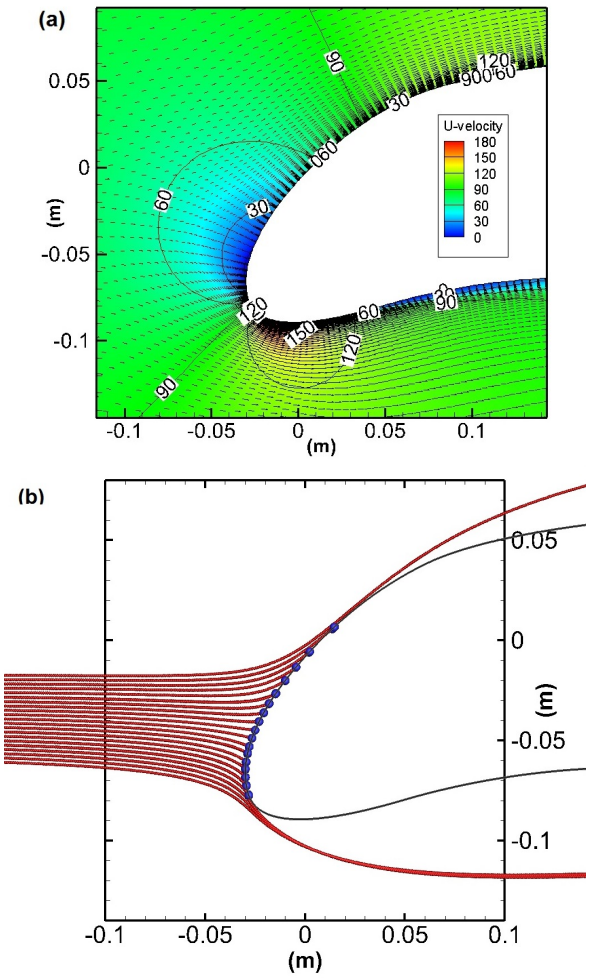

Figure 2. Air flow solution (a) and a sample of drop trajectories and their impingement (b).

Figure 4 shows ice mass as a function of anti-icing heating for the three icing scenarios. Computations of ice shape and its mass were performed for anti-icing heating change increments of 1 kW/m^2. Small black crosses correspond to conditions depicted in Figure 3. Large dots identify critical conditions when ice ceases to form on the heated surface, but it continues to form downstream of the heater.

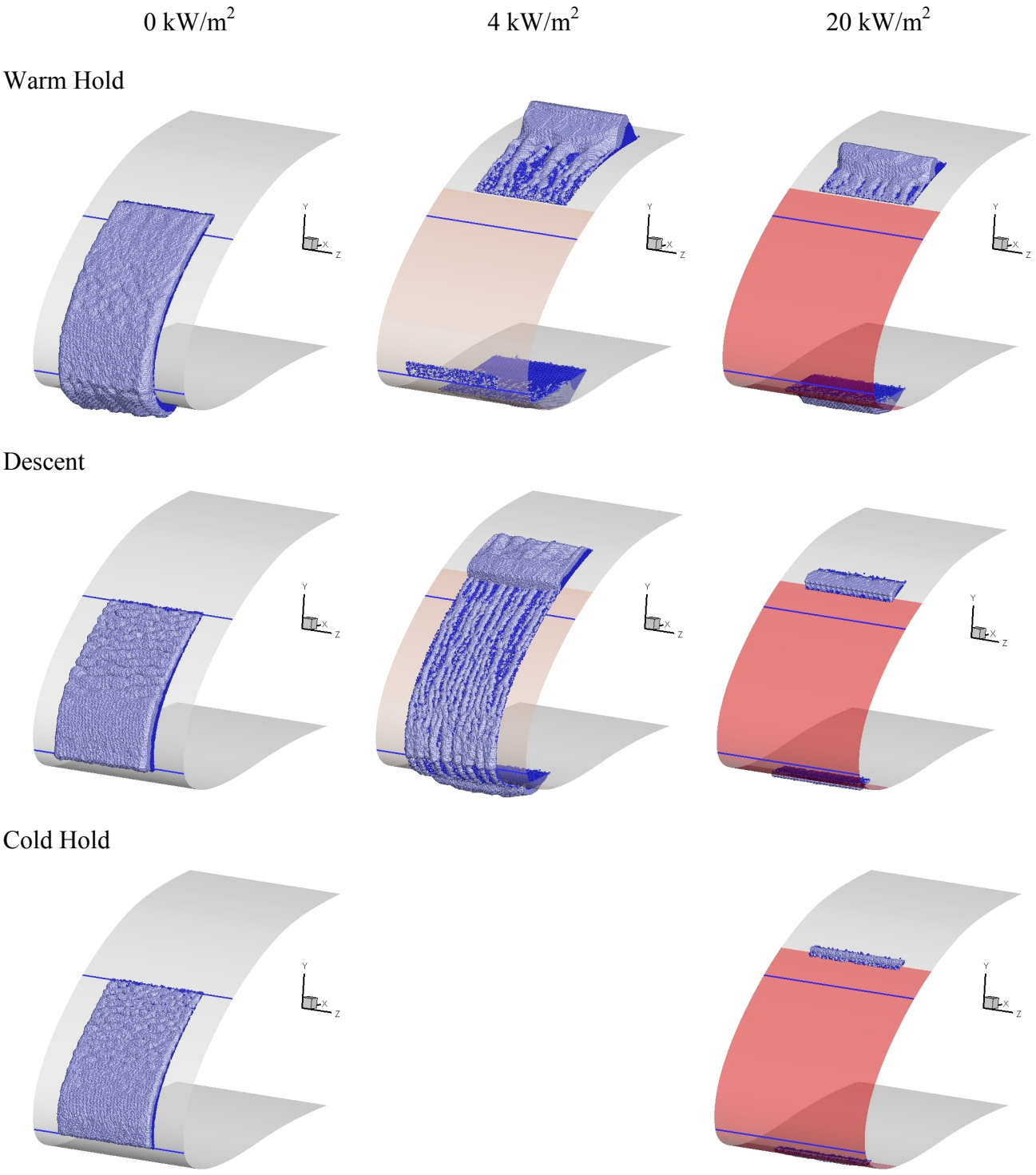

Figure 3. Influence of anti-icing heating of 0, 4 and 20 kW/m^2 on ice accretion shape for Warm Hold, Descent and Cold Hold scenarios. Dark blue and light blue colors depict the ice accretion after two successive 5-min time intervals.

For the Warm Hold scenario, the ice shape without anti-icing heating is shown in the upper left-hand corner of Figure 3. In this case, there is not enough energy to freeze all impinging drops instantly, water flows downstream before freezing, and glaze ice is formed. The runback water crosses the impingement limit line to freeze downstream. The thickness of the resulting ice is rather uniform and the ice surface is comparatively smooth. When anti-

icing heating of 4 kW/m^2 is applied, the unfrozen water flows downstream and a substantial ice accretion forms on the un-heated wing surface. Only a very small accretion forms on the lower part of the heated surface. When anti-icing heating is increased to 20 kW/m^2, the ice accretion mass diminishes from 93% to 46% in comparison with the no-heating case, Figure 4. When heating reaches 32.5 kW/m^2, all water evaporates and ice disappears completely. Water shedding does not occur in any of these cases.

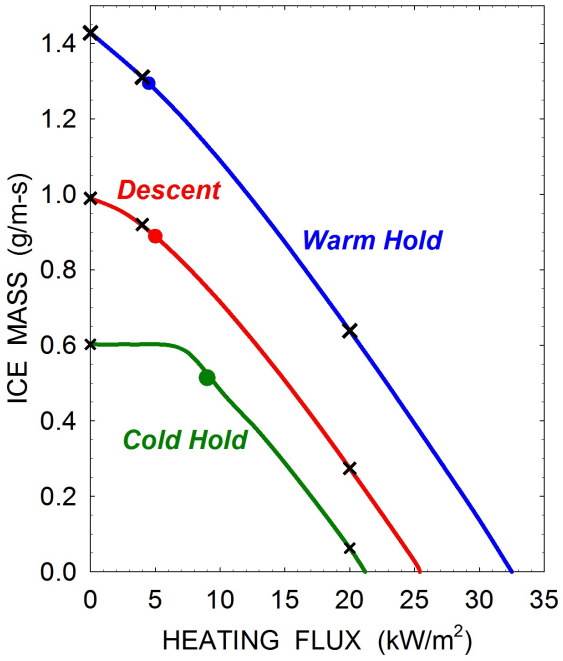

Figure 4. Ice mass flux as a function of anti-icing heating for selected icing scenarios.

The Descent case is characterized by lower air temperatures and a lower liquid water content, leading to a smaller total impinging drop mass. With no anti-icing heating, a glaze ice section near the stagnation line is surrounded by a region of rime with increased surface roughness, see Figure 3. When anti-icing heating of 4 kW/m^2 is applied, runback ice still forms on the heated surface, while unfrozen water leaves the heated region and freezes downstream, forming a pronounced ice layer with a ridge at its leading edge. Due to evaporation, the anti-icing heating reduces the accreted ice mass by 8%. When the anti-icing heating is increased to 20 kW/m^2, ice does not form on the heated surface, but not all of the impinging water mass evaporates and the remaining water freezes downstream, forming a small ice ridges with a mass around 19% of that for the no-heating case. When the heating flux is increased to 25.5 kW/m^2, all of the impinging water evaporates and ice does not form, Figure 4.

Cold Hold is characterized by low air temperature and a smaller impinging drop flux. Consequently, even for the 4 kW/m^2 case, the resulting rime ice accretion is essentially the same as the no-heating ice accretion. Therefore, the ice shape for anti-icing heating of 4 kW/m^2 is not depicted in Figure 3. When the heat flux is increased to 9 kW/m^2, ice no longer forms on the heated surface. This condition is depicted in Figure 4 as a large green dot. A small amount of ice forms just behind the heated surface for a heat flux of 20 kW/m^2, but a further increase to 21 kW/m^2 leads to complete evaporation of all impinging drops and no ice forms on the wing.

These results seem, at first glance, to be counterintuitive, since the largest anti-icing heat flux is required to evaporate water for Warm Hold conditions. This occurs because Warm Hold conditions are associated with high liquid water content that outweighs the influence of the warmer environment.

5 Conclusions

The NRC morphogenetic icing model is able to predict the effect of anti-icing heating on the detailed ice accretion shape forming on a wing. Due to its discrete particle formulation, the model has the unique ability to simulate the formation of rough and complex ice structures, as well as the formation of frozen rivulets and ice ridges. This model can potentially be used in the design of anti-icing devices. It could also be used to help estimate the aerodynamic penalties due to ice accretions, arising from insufficient anti-icing heating.

An increase of anti-icing heat flux leads to an increase in evaporated water mass, a decrease of ice mass and a downstream displacement of the ice centre of mass. The ice mass for a Warm Hold is the largest, because it is associated with the largest liquid water content and flux of impinging drops. By contrast, Cold Hold is

characterized by the smallest ice mass and the smallest critical anti-icing heating flux required to prevent ice formation.

In the future, following further experimental verification, these predicted ice shapes could be manufactured using 3D printers and placed in a wind tunnel for aerodynamic tests.

References

[1] Alègre N and Hammond D. Experimental setup for the study of runback ice at full scale. *Journal of Aircraft*, Vol. 48, No. 6, pp 1978-1983, 2011.

[2] Addy H E, Broeren A P, Oleskiw M and Orchard D. A study of the effects of altitude on thermal ice protection system performance. *Proc 5th AIAA Atmospheric and Space Environments Conference*. San Diego, USA, AIAA 2013-2934, 2013.

[3] Strobl T, Storm S, Thompson D, Hornung M and Thielecke F. Feasibility study of a hybrid ice protection system. *Journal of Aircraft*, Vol. 52, No. 6, pp 2064-2076, 2015.

[4] Orchard D, Addy H E, Wright W B and Tsao J. Altitude scaling of thermal ice protection systems in running wet operation. *Proc 9th AIAA Atmospheric and Space Environments Conference*, Denver, USA, AIAA 2017-3926, 2017.

[5] Broeren A P, Whalen E A, Busch G T and Bragg M B. Aerodynamic simulation of runback ice accretion. *Journal of Aircraft*, Vol. 47, No. 3, pp 924-939, 2010.

[6] Pourbagian M and Habashi W. Surrogate-based Optimization of electrothermal wing anti-icing systems. Journal of Aircraft, Vol. 50, No. 5, pp 1555-1563, 2013.

[7] Szilder K and Lozowski E P. Novel two-dimensional modeling approach for aircraft icing. *Journal of Aircraft*. Vol. 41, No. 4, pp 854-861, 2004.

[8] Szilder K and Lozowski E P. Comparing experimental ice accretions on a swept wing with 3D morphogenetic simulations. *Journal of Aircraft* (in press), 2018.

[9] CFD-FASTRAN *Software Manual*, CFD Research Corporation, Huntsville, AL, 2002.

[10] Szilder K, McIlwain S and Lozowski E P. Numerical simulation of complex ice shapes on swept wings. *ICAS 2006*, Hamburg, Germany, 2006-2.5.1, 2006.

[11] Orchard D. Personal communication, 2017.

Contact Author Email Address

Krzysztof.Szilder@nrc-cnrc.gc.ca

Copyright Statement

The authors confirm that they, and/or their company or organization, hold copyright on all of the original material included in this paper. The authors also confirm that they have obtained permission, from the copyright holder of any third party material included in this paper, to publish it as part of their paper. The authors confirm that they give permission, or have obtained permission from the copyright holder of this paper, for the publication and distribution of this paper as part of the ICAS proceedings or as individual off-prints from the proceedings.